

Simulating the Carbon Footprint of Galactic Halos

Simeon Bird^{1,2*}, Kate H. R. Rubin³, Joshua Suresh³, Lars Hernquist³

¹*Carnegie Mellon University, 5000 Forbes Avenue, Pittsburgh, PA, 15206, USA*

²*Johns Hopkins University, Baltimore, MD 21218, USA*

³*Harvard-Smithsonian Center for Astrophysics, 60 Garden Street, Cambridge, MA 02138, USA*

29 July 2016

ABSTRACT

We compare simulations, including the Illustris simulations, to observations of CIV and CII absorption at $z = 2 - 4$. These are the CIV column density distribution function in the column density range $10^{12} - 10^{15} \text{ cm}^{-2}$, the CIV equivalent width distribution at $0.1 - 2 \text{ \AA}$, and the covering fractions and equivalent widths of CIV 1548 \AA and CII 1337 \AA around DLAs. In the context of the feedback models we investigate, all CIV observations favour the use of more energetic wind models, which are better able to enrich the gas surrounding halos. We propose two ways to achieve this; an increased wind velocity and an increase in wind thermal energy. However, even our most energetic wind models do not produce enough absorbers with CIV equivalent width $> 0.6 \text{ \AA}$, which in our simulations are associated with the most massive haloes. All simulations are in reasonable agreement with the CII covering fraction and equivalent widths around Damped Lyman- α absorbers, although there is a moderate deficit in one bin $10 - 100 \text{ kpc}$ from the DLA. Finally, we show that the CIV in our simulations is predominantly photoionized.

Key words: intergalactic medium – galaxies: formation

1 INTRODUCTION

Understanding the nature of galactic feedback, the manner in which luminous objects such as stars and quasars affect the gas surrounding them, is one of the most significant open problems in galaxy formation. Neither individual supernovae nor black hole accretion discs are resolved in current cosmological simulations, and so they are included through approximate effective models for stellar and Active Galactic Nuclei (AGN) feedback. These models are tuned to produce realistic low-redshift galaxies (e.g. Schaye et al. 2010; Davé, Oppenheimer & Finlator 2011; Puchwein & Springel 2013; Vogelsberger et al. 2013; Schaye et al. 2015). Observations apart from those the models were adjusted to match are also reproduced. For example, the stellar properties of high redshift galaxies (Torrey et al. 2014), the neutral hydrogen column densities in Damped Lyman- α Systems (DLAs) (Bird et al. 2014) or the abundances of Lyman Limit Systems around quasars (Rahmati et al. 2015). Further refining the sub-resolution modeling requires observational probes able to constrain independent parameters and thus inform different elements of the model.

In this paper we examine results from the Illustris Project (Vogelsberger et al. 2014a,b; Genel et al. 2014; Nel-

son et al. 2015), as well as smaller simulations with a different supernova wind energy per unit mass. We compare our simulations to observations of absorption lines from singly and triply-ionized carbon. CII traces relatively dense, low temperature gas closely associated with galactic haloes. CIV traces enriched gas at a density more typical of the intergalactic medium, and thus provides complementary information to measurements characterizing on stars or neutral hydrogen (Haehnelt, Steinmetz & Rauch 1996). Examining both ions helps us to distinguish variations in ionization fraction from variations in enrichment. Suresh et al. (2015b) showed that this parameter affects the distribution of circumgalactic metals, and that an increased energy can help improve agreement with measurements of the CIV column density around $z \sim 2.5$ galaxies (Turner et al. 2014). Here we show that this parameter has further observational consequences.

We first compare our simulations to the line density and column density function of weak (column density $< 10^{15} \text{ cm}^{-2}$) CIV absorbers (D’Odorico et al. 2010).¹ Comparisons of this type have already been used to constrain feed-

¹ These absorbers are sometimes taken to trace the metal content of the Intergalactic Medium (IGM), but Oppenheimer & Davé (2006) showed the two are poorly correlated.

* E-mail: sbird4@jhu.edu

back models. Indeed, Oppenheimer & Davé (2006, 2008) (henceforth OD06, OD08) used data from Songaila (2001); Boksenberg, Sargent & Rauch (2003); Songaila (2005) and Scannapieco et al. (2006) to help motivate the class of supernova feedback models on which the Illustris Project is based. Tescari et al. (2011) expanded the analysis to include the updated data of D’Odorico et al. (2010) and to constrain a broader class of feedback models, including AGN feedback. Most recently, Rahmati et al. (2016) compared the results of the EAGLE simulation to observations of CIV, and other high ionization systems. However, our study will be the first to use CIV to test the feedback model in the Illustris simulation. We focus on comparisons to the dataset presented in D’Odorico et al. (2010) as their survey covers a combined path length of $\Delta X = 86$, the largest CIV survey currently available at high resolution. Furthermore, using a single recent measurement of the CIV column density function allows us to generate simulated spectra which match as closely as possible the properties of the observations.

In addition, we will perform a comparison to other observed properties of CIV. We use the line density of strong CIV absorbers (equivalent width $0.3 - 1.2 \text{ \AA}$) from Cooksey et al. (2013), measured using a large spectral sample of absorbers from the Sloan Digital Sky Survey (SDSS; York et al. 2000). These stronger absorbers allow us to extend the range of our comparison to gas at a density and enrichment found only around large haloes. To check our simulations against smaller haloes traced by high redshift galaxies too faint to be detected in imaging surveys, we compare to the carbon absorption around DLAs as measured by Rubin et al. (2015) using close quasar pairs.

The literature contains various theoretical studies examining how different feedback models influence the properties, ionization state and enrichment of the $z = 2$ IGM and circumgalactic medium (CGM). For example, Cen & Chisari (2011) and Barai et al. (2013) showed that allowing wind strength to vary as a function of galactic radius affects the gas and metallicity profiles. Ford et al. (2013, 2014) found that the CGM at $z = 0.5$ is enriched by cool outflows which then ultimately re-accrete onto the galaxy. By contrast, Shen et al. (2012, 2013) found that at $z = 3$, outflows free-stream out of the potential well of a simulated high resolution galactic halo. Suresh et al. (2015b) showed that these differences arise not only due to the differing redshifts, but also owing to their wind models having different effective energy per unit mass. As the theoretical properties of the CGM have already been extensively examined, we choose to focus here on a comparison to specific observations.

We use observations in the redshift range $z = 2 - 4$, in part because Suresh et al. (2015b) showed that this is the epoch during which the circumgalactic metallicity is most sensitive to the parameters of the supernova model. The gas metallicity and CIV abundance at lower redshifts are controlled by the AGN feedback model and at higher redshifts by the details of reionization. Furthermore, the statistical power of the observational surveys is largest at $z = 2 - 4$. The evolution of the IGM from $z = 2 - 0$ has been examined by Davé et al. (2010), while Oppenheimer et al. (2012) compared their simulations to low-redshift ($z = 0 - 0.5$) metal-line data (Danforth & Shull 2008; Cooksey et al. 2010), and more recently CIV surveys have been carried out at $z < 2$ by (Burchett et al. 2013, 2015). Future work could use these

surveys to constrain AGN feedback models. Constraints on the CIV column density distribution has also been obtained at $z > 5$ by Pettini et al. (2003); Becker, Rauch & Sargent (2009); Ryan-Weber et al. (2009); Simcoe et al. (2011). The implications of our simulations for these observations was examined in Keating et al. (2016).

In Section 2, we describe our simulations and our methods for generating mock observations. Section 3 discusses properties of our simulated absorbers, including their host haloes and the extent to which their ionization state is dominated by photo-ionization. Section 4 presents a comparison to the observations, and we draw conclusions in Section 5. Appendix A shows the convergence of our results with numerical resolution, and Appendix B reproduces in tabular form the results shown in some of our figures.

2 METHODS

In this section we explain our methods, including a brief overview of the simulations (section 2.1) and feedback models (section 2.2). We then describe briefly how we compute our synthetic spectra (section 2.3). Analysis codes specific to this paper are available at https://github.com/sbird/civ_kinematics.

2.1 Simulations

The simulations analysed in this paper are summarized in Table 1. They comprise the Illustris Project and a few variants on its feedback model, originally described in Bird et al. (2014). All simulations were run using the moving mesh code AREPO (Springel 2010), which combines the TreePM method for gravitational interactions with a moving mesh hydrodynamic solver. Each grid cell on the moving mesh is sized to contain a roughly fixed amount of mass, and to move approximately following the bulk motion of the fluid locally. Small-scale mixing is included by allowing gas and metals to advect between grid cells.

The largest simulation we employ, hereafter “Illustris”, is a box with a comoving linear size $75 h^{-1} \text{ Mpc}$ and a comoving gravitational softening length of $\sim 1 h^{-1} \text{ kpc}$. Illustris initially contains 1820^3 dark matter (DM) particles and 1820^3 gas elements. It is described in more detail in Vogelsberger et al. (2014a,b) and Genel et al. (2014). We have also run several smaller simulations, each with a comoving linear size of $25 h^{-1} \text{ Mpc}$, initially containing 2×512^3 resolution elements and having a comoving gravitational softening length of $\sim 1 h^{-1} \text{ kpc}$. They thus have a similar mass resolution to the Illustris simulation but a lesser volume. Illustris has both stellar and AGN feedback, described in detail in Vogelsberger et al. (2013), and summarized in Section 2.2. Our smaller simulations vary parameters of the stellar feedback model, as described in Section 2.2.

2.2 Feedback Models

As described in detail in Vogelsberger et al. (2013), Illustris includes phenomenological models for feedback which aim to capture the unresolved influence of supernovae and AGN on their environment. The parameters of these models

Name	Box Size (Mpc / h)	AGN	κ_w (Eq. 2)	Notes
ILLUS 75	75	Yes	3.7	Illustris simulation
ILLUS 25	25	Yes	3.7	
WARM 25	25	No	3.7	Thermal winds
FAST 25	25	Yes	5.5	

Table 1. Table of simulation parameters. The AGN column shows whether AGN feedback is enabled. κ_w sets the wind velocity. 50% of the wind energy in the WARM simulation is deposited as thermal energy, as explained in the text.

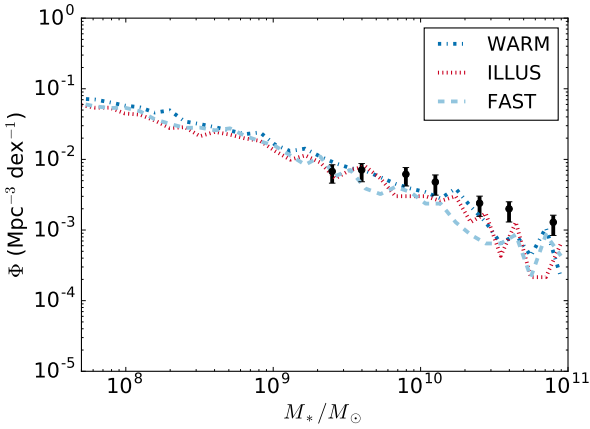


Figure 1. The galactic stellar mass function at $z = 2$ for our three feedback models, WARM, FAST and Illustris, compared to the galactic stellar mass function observed at $z = 2 - 2.5$ by Mortlock et al. (2011). While there are no direct constraints for faint objects at this redshift, all our models agree with the measurements where they overlap. Furthermore each model has a very similar stellar mass function.

have been adjusted to approximately reproduce the galactic stellar mass function and star formation rates at $z = 0$, by suppressing star formation relative to pure gravitational collapse. Mass and energy are returned from star-forming cells to nearby gas cells, adding kinetic and thermal energy and suppressing star formation. This is implemented by star-forming cells stochastically creating wind particles with an energy roughly corresponding to the expected available supernova energy per stellar mass. Wind particles are collisionless. To prevent the wind energy from being quickly dissipated through radiative losses, they are decoupled from hydrodynamic evolution until they reach lower density regions or hit a time limit. At this time they are removed and their energy, momentum, mass and metals are added to the gas cells at their current location. As the hydrodynamic decoupling models the effect of unresolved density fluctuations on the radiative cooling of supernova shock fronts, the parameters of the feedback model should be viewed as being a function of the decoupling time, and must be re-tuned when this changes.

In order to adequately suppress star formation in faint objects, the mass returned from star-forming regions scales with the local velocity dispersion of the dark matter (DM).

The total energy of each wind particle, egy_w , is given by

$$\text{egy}_w = \frac{1}{2} \eta_w v_w^2, \quad (1)$$

where η_w is the wind mass loading and v_w is the wind velocity. egy_w is constant within all our simulations. v_w scales with the local DM velocity dispersion, $\sigma_{\text{DM}}^{\text{1D}}$, which correlates with the maximum DM circular velocity of the host halo (Oppenheimer & Davé 2008). We define

$$v_w = \kappa_w \sigma_{\text{DM}}^{\text{1D}}. \quad (2)$$

The Illustris wind model thus yields large mass loadings in small haloes (as egy_w is constant), which allows it to roughly match the galaxy stellar mass function at $z = 0$ (Okamoto et al. 2010; Puchwein & Springel 2013). The specific parameters chosen yield in Illustris wind ejecta which are frequently not completely unbound from their originating halo. Furthermore, the high mass loading leads to a relatively cold CGM (Suresh et al. 2015b).

The metallicity of the supernova winds is taken to be 0.4 times the metallicity of the star-forming gas launching the wind, following Vogelsberger et al. (2013). We ran a simulation where the supernova wind metallicity was 0.7 times the gas metallicity and checked that this parameter had a negligible effect on to each set of observables we consider. Vogelsberger et al. (2013) and Suresh et al. (2015b) performed similar checks with the same result. This may indicate that the CGM is not enriched by the wind particles themselves, but by outflows accelerated by energy transferred from the wind particles. Note that zero-metallicity winds can affect the dynamical evolution of the CGM over time by reducing the impact of metal cooling (Suresh et al. 2015b). Metal cooling is included as outlined in Vogelsberger et al. (2013).

As shown in Table 1, we consider two variants of this model: faster winds (FAST) and hotter winds (WARM). Both of these have an increased wind energy per unit mass, egy_w/η_w , while the total wind energy, egy_w , is kept fixed. The WARM model offers a way to include thermal energy without altering the stellar mass function. To accomplish this, the wind velocity is held fixed and half the total wind energy is deposited in thermal energy when the wind recouples, following Marinacci, Pakmor & Springel (2014). Thus Eq. 1 becomes

$$\text{egy}_w = \frac{1}{2} \eta_w v_w^2 + \text{egy}_{\text{therm}}. \quad (3)$$

Since egy_w and v_w are held fixed, increasing $\text{egy}_{\text{therm}}$ decreases the mass loading, η_w and hence increases egy_w/η_w . Physically, thermal energy models shocking that may occur in the wind during the phase when it is modelled by a decoupled particle. Suresh et al. (2015b) showed that this wind model does not directly produce hotter gas near the virial radii of our dark matter haloes, a range $50 - 200 h^{-1} \text{kpc}$ from the galaxy. This is because outflows generally shock before reaching this point, even in the Illustris model. However, Suresh et al. (2015b) also showed that the higher energy outflows present in WARM can more easily escape the enclosing halo and enrich the CGM than in Illustris.

The star formation rate in a resolved halo is largely independent of particle mass resolution in all our simulations. Adding extra thermal energy to the winds does not induce a resolution dependence, because thermal wind energy, like kinetic wind energy, is initially hydrodynamically

decoupled from the gas. The feedback model governs how high density material couples to the rest of the simulation, and includes physical processes smoothed to the new density scale introduced by re-coupling. The numerical parameters of the feedback model are implicitly defined as a function of this scale, rather than the mass resolution of the simulation. Thus changing the mass resolution of the simulation does not require recomputing these parameters to achieve the same star formation rate.

Our second parameter variation considers faster winds (FAST). Here we fix the wind energy, eg_{w} , as before, but increase κ_{w} to 5.5, and hence increase the wind velocity v_{w} by 50%. Like warm winds, this enhances the enrichment of the circumgalactic medium (Suresh et al. 2015b). As shown in Vogelsberger et al. (2013), increasing the wind speed can reduce star formation at low redshifts, as faster outflows are more rarely re-accreted onto haloes. To avoid this, we increase the wind speed by a moderate factor of 1.5, which enriches the CGM but, as shown by Figure 1, does not affect the galaxy stellar mass function at $z \geq 2$.

Figure 1 shows the galaxy stellar mass function for all three of our feedback models. Each feedback model yields similar results. The reduced wind mass loading in the WARM winds model weakens the strength of the feedback and slightly increases the stellar mass, while the faster winds in the FAST model have the opposite effect, especially for larger halos. All three models agree well with the limited observational data available at this redshift. We have also checked that the stellar metallicities are similar for each model. In Bird et al. (2014) we showed that all three models produce similar abundances and metallicities for Damped Lyman- α systems, strong neutral hydrogen absorbers. Thus none of our feedback models change the stellar or neutral gas properties of the simulation. However, as explained in Appendix B2 of Suresh et al. (2015b), the default wind model of Vogelsberger et al. (2013) launches winds with a characteristic energy close to the virial temperature of the host halo. Both our parameter variations increase the energy per unit mass available to the outflows by approximately a factor of two, and thus launch winds exceeding the potential energy of their host halo that can enrich the circumgalactic medium to greater distances.

AGN feedback was disabled in the WARM winds model, to test the extent to which CIV abundance at $z = 2$ is sensitive to the AGN. As implemented in Illustris, AGN feedback suppresses star formation in the most massive haloes by periodically releasing thermal energy from the black hole into the gas cells surrounding it. The amount of energy released is chosen to be sufficiently large to avoid being dissipated through radiative cooling in the dense gas immediately surrounding the black hole (Di Matteo, Springel & Hernquist 2005; Springel, Di Matteo & Hernquist 2005; Sijacki et al. 2007; Vogelsberger et al. 2013). The heating effect of AGN feedback substantially reduces the gas density within the host halo (van Daalen et al. 2011). The gas expelled from the halo enriches the circum-galactic medium with metals (Tescari et al. 2011; Suresh et al. 2015b). However, we shall show that the effect of enrichment due to AGN feedback on the observations we consider is relatively small. This is partly because the larger haloes hosting AGN are relatively rare at $z = 2 - 4$, and partly because the ejected gas

is heated beyond the temperature where it can produce a strong CIV absorption signal.

Gas is enriched both by nearby star particles and by supernova winds. Enrichment events are assumed to occur from asymptotic giant branch stars and supernovae, with the formation rate of each calculated using a Chabrier (2003) initial mass function. The elemental yields of each type of mass return are as detailed in Vogelsberger et al. (2013). Metals are distributed into the gas cells surrounding a star using a top-hat kernel with a radius chosen to enclose a total mass equal to 256 times the gas element mass targeted by the refinement algorithm (see Vogelsberger et al. 2013). This models the expansion of the metals from the initial stellar event during the first timestep. To ensure that our results are not sensitive to this parameter, we ran a simulation where metals were distributed within a radius enclosing 16 times the gas element mass, with minimal changes to our results. Advection apparently erases the effect of the enrichment radius on short time-scales.

2.3 Artificial Spectra

To compute the absorption profile along sightlines in our simulations, we need to calculate the ionization fraction of carbon ions within each gas cell. We use a lookup table generated by running CLOUDY, version 13.02 (Ferland et al. 2013), as described in Bird et al. (2015) and publicly available at https://github.com/sbird/cloudy_tables.

CLOUDY is run in single-zone mode, which assumes that the density and temperature are constant within each gas element. We thus neglect density and thermal structure on scales smaller than the resolution limit of each simulation, which is consistent as this structure would be unresolved by definition. When generating simulated spectra, the ionization fraction is computed for each gas cell using the lookup table.

We assume ionization equilibrium and the presence of a uniform radiation background following Faucher-Giguère et al. (2009). We have checked explicitly, using a separate simulation where the amplitude of the radiation background was increased by a factor of two, that our results are insensitive to the background amplitude within current observational uncertainties.

Oppenheimer & Schaye (2013) examined the effects of non-equilibrium cooling on the CIV fraction and we have checked using the ionization tables they provide that the difference in CIV fraction between equilibrium and non-equilibrium ionization for gas with $Z \sim 0.3Z_{\odot}$ at $z = 2$ is $\sim 10\%$, negligible for our purposes. This overestimates the impact; almost all the absorbing gas is at lower metallicity where the effect is much smaller. We neglect the impact of local ionizing radiation from stellar sources. Suresh et al. (2015a) showed that for a $10^{12}M_{\odot}$ halo this has an effect only < 50 kpc from the galaxy at $z = 0.2$. Figures 4 and 5 shows that most of our absorbers are at distances > 100 kpc from the center of a halo, and found near halos with $< 10^{11}M_{\odot}$, so we do not expect local sources to have a significant effect.

We account for shielding from the radiation background at high hydrogen column densities, as described in Bird et al. (2015). We have checked that this has no effect on CIV, but substantially increases the abundance of CII. We model the

onset of shielding using the fitting function from Rahmati et al. (2013), who used a radiative transfer scheme to estimate the threshold hydrogen density for gas to become neutral. This fitting function is implemented in AREPO, so that the effect of self-shielding on hydrogen cooling is included in the dynamics of the simulation. A rule of thumb is that gas becomes neutral at $\gtrsim 0.01 \text{ cm}^{-3}$ with our redshift 2 UVB. Shielding for metal species is reduced at high energies by a frequency dependent correction to model the reduced cross-section of hydrogen photoionization to high photon energies, as explained in Bird et al. (2015).

The thermodynamics of dense, star-forming gas is set by the subgrid model for star formation (Springel & Hernquist 2003). This assumes that star-forming gas has a temperature $\sim 10^4 \text{ K}$ and thus contains negligible CIV and substantial CII. Higher resolution simulations could reveal shocks in this dense gas, heating some of it to a temperature closer to the 10^5 K necessary to form CIV via collisional ionization, and increasing the global abundance of high column density CIV systems. Modelling this effect is beyond the scope of our present paper, but the relatively small covering fraction of star-forming gas suggests that changes in the CIV absorption statistics are small.

The effective aperture of a physical quasar sightline, $< 1 \text{ pc}$, is much smaller than the maximum spatial resolution of our simulations, $\sim 1 \text{ kpc}$. We neglect any observational effects which may arise due to spatial structure on these small scales. However, we shall show that the carbon absorption we consider here is produced in warm, diffuse circumgalactic gas which does not exhibit substantial structure on small spatial scales. While dense spatially compact clumps unresolved by our simulations may exist, we expect them to be confined to the high density inner regions of galaxies, where they can be sufficiently shielded from the UVB to collapse. They would thus have a small covering fraction. We acknowledge, however, that recent observations (e.g. Crighton et al. 2015), may suggest otherwise, but resolving this problem is beyond the scope of this work.

Our artificial spectra are generated as described in detail in Bird et al. (2015), using the implementation available at https://github.com/sbird/fake_spectra. Once the mass of the desired ion in each gas element has been computed, it is interpolated onto a sightline using a Voigt profile convolved with an SPH kernel. The b -parameter of the Voigt profile is set by the temperature of the particle, naturally including thermal broadening. Each gas element is redshifted by its velocity parallel to the sightline, naturally accounting for peculiar velocities. Generated sightlines are noiseless. The size of a spectral pixel is 5 km/s when comparing to D’Odorico et al. (2010) and Cooksey et al. (2013) and 50 km/s when comparing to Rubin et al. (2015).

We compute column densities primarily by interpolating the mass of the desired ion in each gas element to the sightline, as for the optical depth. Unlike when computing the optical depth, we do not redshift the particle according to its peculiar velocity, and use a top-hat spherical kernel rather than a Voigt profile. Thus our column densities correspond to the integrated physical density field in the simulation, and allow us to examine the physical state of the absorber. This differs from common observational practice, which uses a Voigt profile fit from the optical depth. However, we have checked with a subset of our simulated spectra

that performing Voigt fitting on the artificial spectra to estimate the column densities does not affect our results.

3 ABSORBER PROPERTIES

Figure 2 shows the column density in CII and CIV around a typical simulated halo in both our warm winds and Illustris simulations, with a mass of $6 \times 10^{10} h^{-1} M_{\odot}$ at $z = 2$. The column density is calculated by projecting the mass in each particle using a spherical top-hat kernel onto a gridded cube $300 h^{-1} \text{ kpc}$ across and centred on the halo. We have split the colour of CIV absorption by column density thresholds. The transition between yellow and blue at 10^{12} cm^{-2} marks the lowest column density observable by D’Odorico et al. (2010). The transition between red and yellow marks $W_{1548} \approx 0.2 \text{ \AA}$ ($N_{\text{CIV}} \approx 2 \times 10^{14} \text{ cm}^{-2}$), the detection threshold in Rubin et al. (2015). In this halo, the strongest CII absorbers are associated with dense clumps of cool material, also producing strong HI absorption. Observable CII absorbers are present at similar levels in both simulations, but CIV absorption is significantly more extended in the WARM simulation.

Figure 3 shows two examples of simulated CIV spectra from our WARM simulation, and we have examined several more CIV absorption profiles by eye. We chose these examples to illustrate that our CIV spectra sometimes contain considerable structure. While weaker absorbers tend to have simple Gaussian profiles, CIV systems with column density $> 10^{14} \text{ cm}^{-2}$ are especially complex. Absorption profiles often contain multiple features, sometimes overlapping and in other cases separated by a few hundred km/s . This is mirrored in real spectra at high enough resolution (e.g. Haehnelt et al. 1996), and in some of the stronger systems in D’Odorico et al. (2010). However, the relatively low resolution of the SDSS spectra from which the observed strong absorber sample is drawn produces smoothed profiles (Cooksey et al. 2013).

3.1 Host Halos

In Bird et al. (2014) we associated DLAs to the dark matter halo in which they were found. However, a substantial fraction of $N_{\text{CIV}} > 10^{12} \text{ cm}^{-2}$ absorbers in our simulations at $z = 2$ are located outside of any halo. Since gas is enriched by stellar activity, one solution would be to assign an absorber to the halo which contains the majority of the stars which caused the enrichment. However, in our moving mesh simulations material is allowed to move between neighbouring gas cells, and so it is difficult to track the ultimate source of metals. Illustris contains an implementation of stochastic tracers designed to solve this problem (Genel et al. 2013). Unfortunately, we found that because these tracers follow the total gas mass, they did not provide adequate sampling of the metal flow. Re-running Illustris with metallicity tracers is beyond the scope of our current paper.

Instead we assign absorbers to the largest halo within 400 physical kpc , chosen as the minimum distance which assigned a halo to 99% of absorbers. This matches the practice of observers, who often connect absorbers with the brightest object within some physical distance. We make the approximation that the brightest object corresponds to the most massive halo, which is reasonable at these redshifts

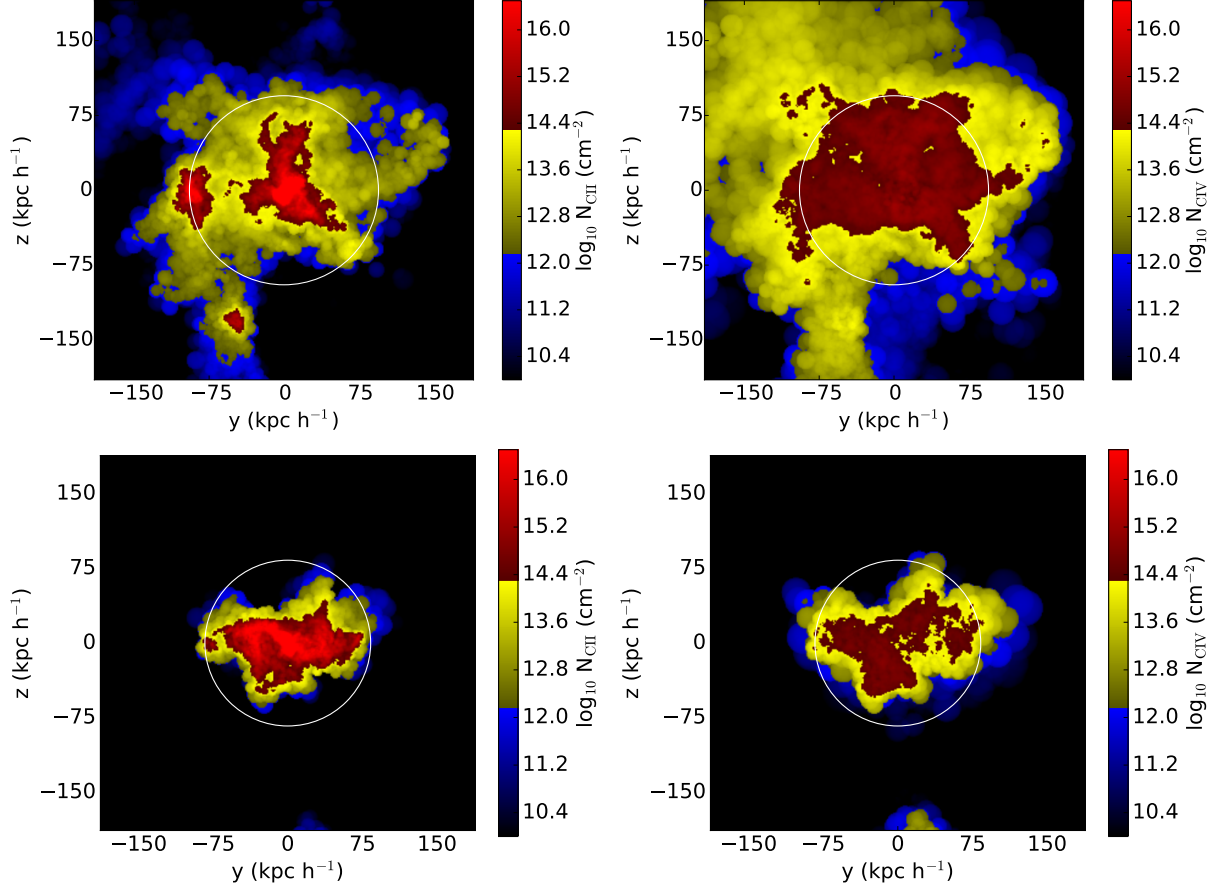


Figure 2. Top: Column densities around a typical DLA-hosting halo in the WARM simulation at $z = 2$. Bottom: Column densities around a typical DLA-hosting halo in the ILLUS 25 simulation at $z = 2$. The halo has mass $\approx 6 \times 10^{10} h^{-1} M_{\odot}$ and the white circle marks the halo virial radius. Left: CII column density. Right: CIV column density. In WARM, both CIV and CII are present at detectable levels throughout the halo, up to the virial radius. In the fiducial model, there is a lack of weak absorbers as the winds do not enrich gas outside the halo. The circular features are artefacts of our spherical projection kernel.

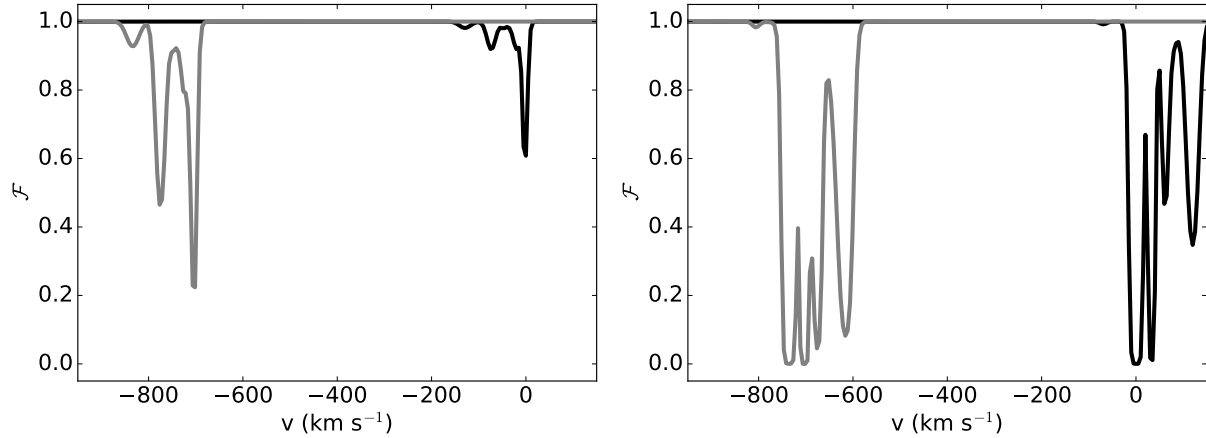


Figure 3. Two example CIV spectra, from the WARM simulation at $z = 2$. The 1550 Å line is shown in black, while the 1548 Å doublet is overlaid in grey. (Left) an unsaturated absorber. (Right) a saturated line with a maximum optical depth $\tau > 4$.

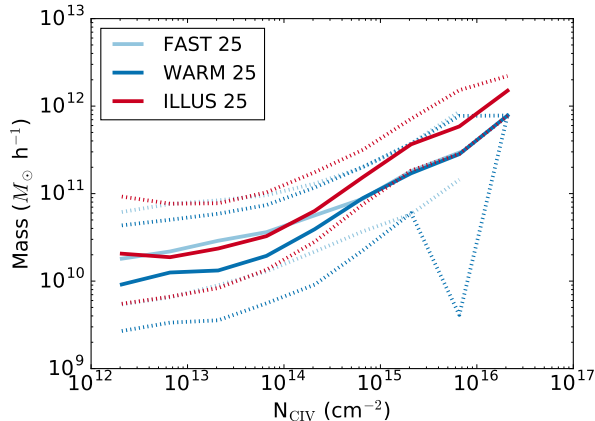


Figure 4. Distribution of associated halo mass for different CIV column densities at $z = 2$ in the Illustris and WARM winds simulations. Solid lines show the median in each column density bin, while dotted lines show the upper and lower quartiles. Strong absorbers, while extremely rare, are found predominantly in the largest halos, while weak absorbers are associated with a wide range of halos.

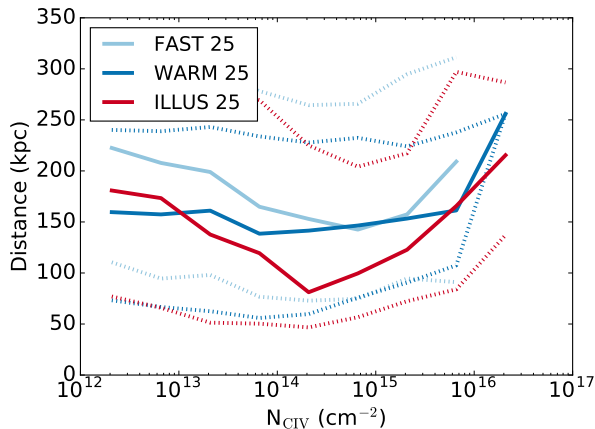


Figure 5. Distribution of distances (in proper kpc) of CIV absorbers from their assigned host haloes at $z = 2$ in the Illustris and WARM winds simulations. Solid lines show the median in each column density bin, while dotted lines show the upper and lower quartiles.

where relatively few galaxies are quenched. An alternative would be to weight distances by the virial radius of the halo concerned. This gives similar results, but given the observational difficulty of determining virial radii we decided against it. Reducing the maximum distance naturally reduces the mean distance from the absorber somewhat but does not change trends, as long as a threshold $\gtrsim 250$ kpc is chosen. Interestingly, this is roughly the mean distance between 10^{16} cm^{-2} absorbers and their host halo. The redshift of an absorber along a sightline is given by the mean CIV mass-weighted redshift. Our prescription will generally prefer larger haloes, which dominate the dynamics of a group, and, at $z = 2 - 3.5$, the global star formation rate. Many CIV absorbers are also close to small haloes; with a low star formation rate, these haloes should not sub-

stantially affect overall enrichment, so our halo assignment procedure ignores them by design.

Figure 4 shows the mass distribution of CIV absorber host haloes at $z = 2$. Absorber column densities are computed as described in Section 4.1. Most weak CIV absorbers are found around small haloes, which are more common, but weak absorbers are also found around larger halos. By contrast, absorbers with $N_{\text{CIV}} \gtrsim 10^{15} \text{ cm}^{-2}$ are found only in haloes with mass $> 10^{11} h^{-1} M_{\odot}$. Figure 5 shows the mean distances of absorbers from the selected host halo, emphasising that absorbers of all strengths can be found at distances much larger than the virial radius of the halo we associate them with, which ranges between 300 and 50 kpc. The large distances found in these figures show that the more energetic winds are especially able to launch material further from the host halo, and thus produce CIV absorption at larger distances. Indeed, the energy per unit mass of the wind ejecta in many cases exceeds the potential energy of the halo. This spreads the material over a wider region and we shall see that it substantially boosts the abundance of CIV absorbers. The increased enrichment also means that strong absorbers can occur around smaller haloes than in the Illustris simulation. Note there is large scatter in the halo-absorber distance, as CIV absorption is produced by gas at a range of densities in a variety of spatial locations, rather than being confined to dense self-shielded gas at the center of a halo.

To aid interpretation of our comparison to the results of Rubin et al. (2015) in Section 4.3, Figure 6 shows the median radial carbon column density profile for our simulated DLAs. The column density is shown as a function of the perpendicular distance between paired sight-lines. Column densities are computed by integrating the density along the non-DLA sightline within 300 km/s of the DLAs peculiar velocity. Sight-line pairs are chosen so that at least one of each pair contains a DLA, but no other condition is placed on the material between the sight-lines. The shown profiles are averaged over $z = 2 - 3$. These choices model the selection function used in Rubin et al. (2015), and are discussed further in Section 4.3. Less than 20 kpc from the DLA, the most common ionization state is CIII. Near the DLA the gas is cool and dense and absorbs in HI. Further away from the DLA the dominant ionization state changes to CIV and CV. CV is not easily observable in absorption, so this phase is observed most easily as CIV.

The density profile is dependent on the wind model. FAST is omitted as its profile strongly resembles WARM. Profiles in WARM and FAST are flatter than in Illustris. The effect of the increased energy in the WARM winds simulation is to boost the abundance of all carbon ions more than $30 h^{-1} \text{ kpc}$ from the DLA, although only the increase in CIV is observable. As discussed further in Section 4.3, this is due to the higher energy winds, which are able to launch metals out of the star-forming regions where they originate more easily.

3.2 Ionisation balance

Figure 7 shows the CIV ionization fraction for a range of temperatures and densities. At temperatures $T \sim 10^5 \text{ K}$ and densities $\rho > 10^{-3} \text{ cm}^{-3}$, CIV is produced by collisional ionization, while at $T < 20000 \text{ K}$ and $\rho = 10^{-4} - 10^{-3} \text{ cm}^{-3}$ CIV is produced by photoionization. The black dashed

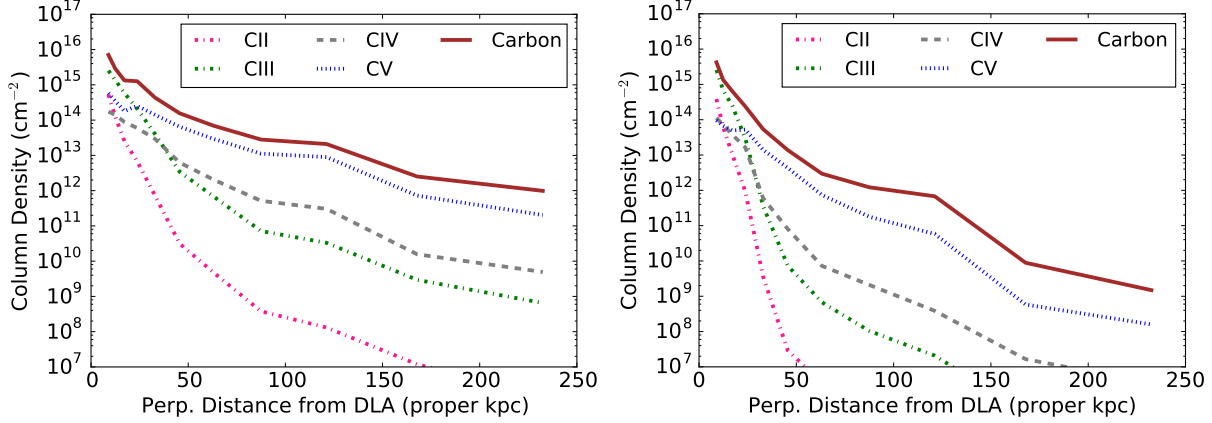


Figure 6. Median column density for carbon ions as a function of perpendicular distance between paired sight-lines, one containing a DLA. Sight-line pairs are selected following Rubin et al. (2015), as explained in the text. Left: the WARM winds $25 h^{-1}$ Mpc simulation. Right: the Illustris $25 h^{-1}$ Mpc simulation. Near the DLA the gas is dominated by CII and CIII, while further away CV is the most common ion. As the column density shows the density integrated along the sightline, some ions are at slightly different redshifts than the DLA. Because CIV and CV are more often separated from the DLA, projection effects may boost their calculated abundances near the DLA relative to CII. We compare to observations in Section 4.3.

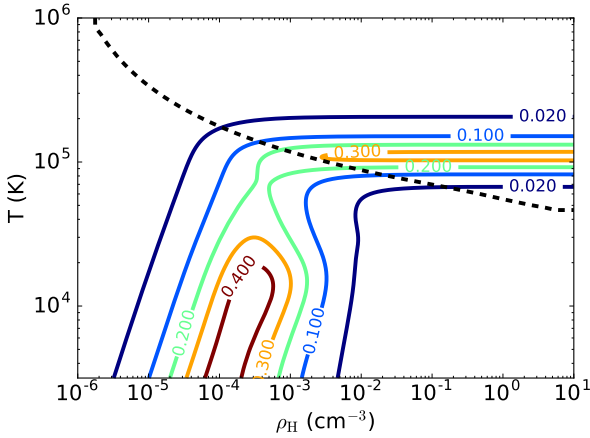


Figure 7. Contours show regions of the temperature-density plane at $z = 3$ where the mass fraction of carbon in CIV is above 0.01, 0.1, 0.2, 0.3 and 0.4, respectively. CIV occurs in a collisionally ionized phase at $T \sim 10^5$ K and a photo-ionized phase at $\rho \sim 10^{-4} \text{ cm}^{-3}$. The black line shows the boundary between the two phases: collisional ionization dominates above the line, photo-ionization below it. At $z = 2$ the maximum CIV fraction in the photo-ionized region is increased by approximately 20%, due to the increased UVB amplitude.

line in Figure 7 shows the boundaries between these two regimes as a function of temperature and density. To compute this boundary, collisional and photo-ionization rates at each temperature and density are tabulated using CLOUDY. The photo-ionization rate depends on the density and the amplitude of the radiation background, while the collisional ionization rate depends on the temperature and density of the material. Higher densities are collisionally dominated at lower temperatures, as the increase in particle density produces more collisions.

As we have access to the physical states of absorbers in the simulations, we are able to determine how much of the mass in CIV absorbers is in each phase. We first com-

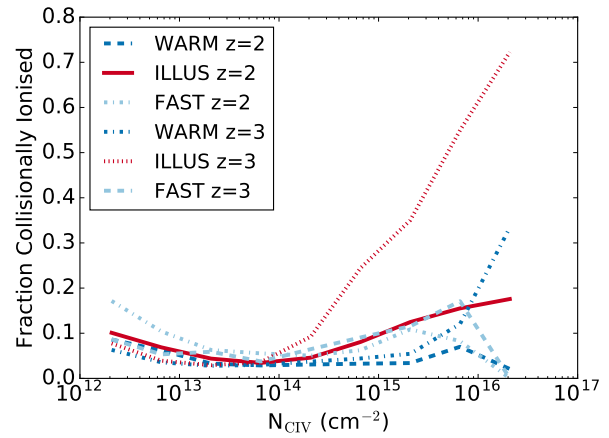


Figure 8. The fraction of CIV which is collisionally ionized as a function of column density. Shown are our three feedback models at $z = 3$ and $z = 2$. Note that although collisionally ionized material in some cases dominates the strongest absorbers, the abundance of these absorbers is low. Overall most CIV absorbers are photo-ionized.

pute whether each gas cell is in a collisionally or photoionized regime, based on its position in the temperature-density plane. We then compute the CIV column density of all collisionally ionized cells by integrating the CIV density of each particle along the sightline, and divide by the total column density. We thus obtain the fraction of CIV absorption from collisionally ionized sources in each absorber. One advantage of this definition is that it avoids projection and smoothing effects by using the temperature and density of the gas cell directly, rather than these quantities averaged over a spectral pixel. This is important because the ionization fraction depends non-linearly on the temperature. Thus the collisional ionization rate for the averaged temperature is not necessarily close to the average of the collisional ionization rates from each particle.

Figure 8 shows the fraction of CIV which is collisionally

ionized as a function of column density. Overall, the collisional ionization fraction of CIV is low: $\sim 4\%$ for WARM and $\sim 6\%$ for ILLUS. This is because the number density of CIV absorbers is dominated by the lower column densities, which are heavily photoionized. Stronger absorbers have a higher collisional fraction, especially with the default Illustris wind model, and at $z = 3$. This is because these strong absorbers are often associated with self-shielded gas, for which the photoionization rate drops to zero. At higher redshift, the UVB amplitude is lower, and gas self-shields at a lower density, so a higher fraction of the absorbers are collisionally ionized.

At all redshifts, the warm winds simulation shows a substantially lower fraction of collisionally dominated absorbers. Most of the collisionally ionized absorbers are still present, but the warm winds model heats the gas, better enabling it to free-stream out of the halo, and leading to additional CIV absorption. As this arises predominantly from low density photo-ionized material, it decreases the fraction of absorbers that are collisionally ionized. We shall see that this property of the wind model also allows it to better match observations, suggesting that, physically, even strong absorbers are largely photoionized.

OD06 found a moderately higher fraction of collisionally ionized CIV absorbers than in our simulations. This appears to be due to our differing definitions of collisional ionization, and does not reflect a change in the physical properties of the gas. OD06 use a simple temperature threshold of 10^5K for densities above 10^{-5}cm^{-3} and reduced temperature thresholds for lower densities, resulting in a much larger region of collisional ionization. We regard our definition as more physical. In particular, lower densities should require higher temperatures to be collisionally dominated.

4 COMPARISON TO OBSERVATIONS

In this section we compare the results of our simulations to observations. We have created simulated CIV measurements comparable to three observational surveys. Section 4.1 compares to D’Odorico et al. (2010), who observed weak CIV absorption in randomly selected quasar sightlines. Section 4.2 compares our results to observations of strong absorber systems (Cooksey et al. 2013). Finally, section 4.3 compares the CIV and CII absorption around DLAs (used as a tracer of the galaxy population) to the results of Rubin et al. (2015).

4.1 Column Density Distribution of Weak CIV Absorbers

We define the column density distribution, $f(N)$, such that $f(N)$ is the number of absorbers per unit column density per unit absorption distance with column density in the interval $[N, N + dN]$. Thus,

$$f(N) = \frac{F(N)}{\Delta N \Delta X(z)}, \quad (4)$$

where $F(N)$ is the number of absorbers along simulated sightlines in a given column density bin. $\Delta X(z)$ is the absorption distance per sightline, defined to account for evo-

lution in line number density with the Hubble flow:

$$X(z) = \int_0^z (1+z')^2 \frac{H_0}{H(z')} dz'. \quad (5)$$

For a box of co-moving length ΔL we use the approximation $\Delta X = (H_0/c)(1+z)^2 \Delta L$ (Bahcall & Peebles 1969).

Ω_{CIV} is the integral of the first moment of the CDDF:

$$\Omega_{\text{CIV}} = \frac{12m_{\text{P}}H_0}{c\rho_c} \int_{10^{12}}^{10^{15}} N f(N, X) dN. \quad (6)$$

ρ_c is the critical density at $z = 0$ and m_{P} is the proton mass. To ensure a fair comparison, the column density limits of $10^{12} - 10^{15}\text{cm}^{-2}$ have been chosen to match those used in D’Odorico et al. (2010)². The lower limit corresponds to the level below which their survey can no longer correct for completeness, while the upper limit is set by the small sample of higher column densities.

We generated a simulated catalogue using 10,000 synthetic sightlines positioned at random through each simulation snapshot. Sightlines with a CIV column density less than 10^{12}cm^{-2} were discarded until we had a sample of 10000 sightlines containing observable CIV absorbers. Average abundances included the path length for the discarded spectra, effectively treating them as non-detections. We compute column densities by summing densities over 50km s^{-1} intervals along the synthetic spectra. This differs from D’Odorico et al. (2010), who measured column densities by fitting Voigt profiles to spectral lines and combining absorbers closer than 50km s^{-1} . We have however checked that the difference between our direct summation of the density field and a full Voigt fit is small. We also checked that our results were unchanged when combining absorbers 150km s^{-1} apart. The absorption in most sightlines arises from gas in a relatively small spatial area, although this gas frequently has a complex velocity structure which leads to a more dispersed absorption profile.

Figure 9 compares our simulations to the measurements of D’Odorico et al. (2010). These include the column density distribution function (CDDF) of weak CIV absorbers and the evolution of the matter density in CIV, Ω_{CIV} . The CDDF measured by D’Odorico et al. (2010) is computed from absorbers over a wide range in redshift, $1.6 < z < 3.6$. To approximate the redshift distribution of the survey, we average the CDDF from different simulation snapshots at $z = 2 - 3.5$, weighted by the fraction of the total path length in each redshift bin in the observational survey. Note that, as other observational surveys have a different redshift distribution and selection function, it is not strictly correct to compare the simulated CIV CDDF shown in Figure 9 to the results of other surveys.

As shown in Figure 9, all our simulations agree well with the shape of the CDDF, and evolve similarly with redshift. By comparing 75 and $25 h^{-1}\text{Mpc}$ boxes we show that, as expected from the results of OD06, a $25 h^{-1}\text{Mpc}$ box is sufficiently large to model CIV systems at these column densities.

However, the Illustris feedback model produces too little

² Rahmati et al. (2015) integrated from 0 to ∞ . Illustris has more strong systems with $N_{\text{CIV}} > 10^{15}\text{cm}^{-2}$ than EAGLE, so for our simulations this would over-estimate the observed Ω_{CIV} by a factor of 2 – 4.

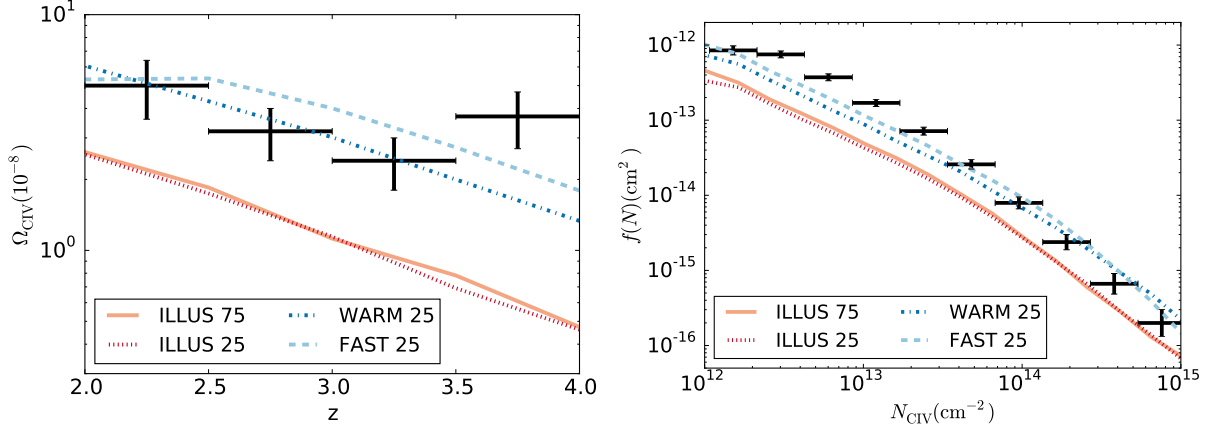


Figure 9. Left: The evolution of Ω_{CIV} , the integrated CIV CDDF between column densities of 10^{12} and 10^{15} cm^{-2} in the simulations considered here. Right: The column density function, $f(N)$, of CIV in the same column density range, averaged over redshifts $2.0 < z < 3.5$. Points with error bars show the measurements of D’Odorico et al. (2010). The WARM and FAST models match observations substantially better than the Illustris model.

CIV by a factor of about 2, as measured both by Ω_{CIV} and the amplitude of the CDDF. FAST and WARM, the more energetic wind models, both produce increased CIV enrichment and thus agree better with observations of Ω_{CIV} and match the CDDF for CIV column densities $> 10^{13} \text{ cm}^{-2}$. They still produce too few of the lowest column density systems. However, as shown in Appendix A, increasing the resolution of the simulation also moderately increases the CDDF for $N_{\text{CIV}} < 10^{13} \text{ cm}^{-2}$, due to star formation in newly resolved halos. A higher resolution version of the WARM or FAST simulation may thus be in agreement with the observed faint end CDDF.

Both WARM and FAST drive more energetic outflows that allow the metals to more easily escape the host halo, and have similar wind energy per unit mass, shown by Suresh et al. (2015b) to be the feedback parameter with most influence on the metallicity of the circumgalactic medium. That they produce similar results suggests that the statistical properties of CIV thus far observed are sensitive only to how much energy is transferred to the circumgalactic gas, not how it is transmitted. We have checked that the effect of AGN feedback is mild for these lower column density systems.

OD06 and OD08 adopt winds with a mass loading $\eta \sim v_w^{-1}$, where v_w is the wind velocity. Illustris on the other hand uses $\eta \sim v_w^{-2}$, and so has a wind mass loading which increases more steeply in lower mass haloes. OD06 increase the mass loading in small haloes by allowing the wind speed to depend on metallicity, so that a lower metallicity induces a higher wind velocity. Overall this leads to an increase in energy per unit mass which boosts Ω_{CIV} by about 50% compared to Illustris. The difference between Illustris and OD06 is slightly smaller than that between Illustris and the observations, as D’Odorico et al. (2010) measures a CDDF with a larger amplitude than the earlier measurements (e.g. Songaila 2001) matched in OD06.

Figure 10 shows the CIV column density function from the $z = 2$ output of our WARM simulation, compared to the results of Oppenheimer et al. (2012) and the EAGLE simulation (Rahmati et al. 2015). Note that each simulation group

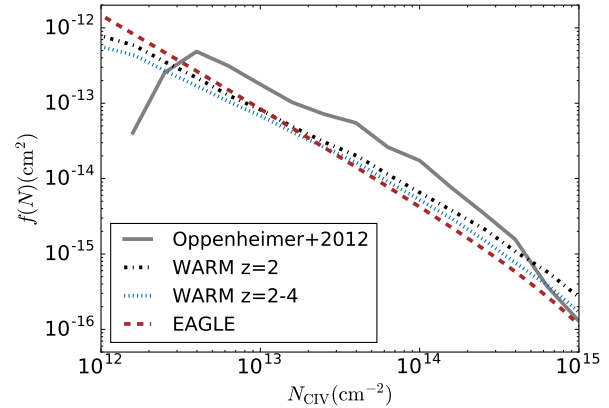


Figure 10. The CDDF from our WARM model at $z = 2$ (dotted) compared to the EAGLE simulation at $z = 2$ (Rahmati et al. 2015) (dashed) and the redshift averaged $z = 1.5 - 2$ CDDF from Oppenheimer et al. (2012) (solid). Note that these results are not directly comparable to the observational data from D’Odorico et al. (2010), as the spectra are not sampled to match the redshift distribution of that survey. We show the redshift-sampled WARM model (dotted) to quantify the size of this effect.

computes the column density function slightly differently. Our methods are described above. Oppenheimer et al. (2012) generated fake spectra in a similar way to us, but computed the column density by Voigt profile fitting. Rahmati et al. (2015) instead projected the simulated CIV density in the simulation box onto a cuboid grid, and computed the column density in each grid cell of volume $(1 \text{ kpc})^2 \times 200 \text{ km/s}$. We do not expect these differences to be significant compared to the different feedback and simulation methods employed. All simulations produced reasonably similar results. In particular, WARM and EAGLE agree remarkably well at low column densities, $N_{\text{CIV}} < 14 \text{ cm}^{-2}$. Regrettably both produce fewer absorbers than are observed at these column densities. Interestingly, EAGLE produces substantially fewer strong absorbers than WARM, which agrees well with the data in this column density range. Oppenheimer et al. (2012) produce the most absorbers with $N_{\text{CIV}} < 14 \text{ cm}^{-2}$,

and is the only model to slightly over-produce the observed CIV CDDF. As explained in their paper, their metallicity-dependent wind model is very effective at enriching the CGM. Note that both simulations produce substantially fewer $N_{\text{CIV}} > 15 \text{ cm}^{-2}$ absorbers than our WARM model; thus we expect both simulations to produce far fewer of the strong absorbers examined in Section 4.2. The difference between the CDDF sampled to match the redshift distribution of D’Odorico et al. (2010) and the $z = 2$ simulation output is comparable to the difference between EAGLE and WARM.

4.2 Equivalent Width Distribution of Strong CIV Absorbers

Cooksey et al. (2013) detected and characterised a large sample of CIV absorbers in the redshift range $z = 2 - 4$ using SDSS spectra. The size of their catalogue allows them to constrain the statistics of strong absorbers. However, each individual SDSS spectrum is of relatively low quality, and so this survey suffers from incompleteness for absorbers with equivalent widths $W \lesssim 0.3 \text{ \AA}$. We compared this data to the same simulated catalogue as in Section 4.1; 10,000 synthetic sightlines, with a CIV column density greater than 10^{12} cm^{-2} , positioned at random through each simulation snapshot. We checked that sample variance was negligible for our simulated sample.

We define the CIV equivalent width, W_{1548} , as the integral of the normalized flux along the sightline

$$W_{1548}(\tau) = \int 1 - \exp(-\tau) dv. \quad (7)$$

The integration range was initially $-400 < v < 250 \text{ km s}^{-1}$ from the center of the absorber, which was defined as the velocity of the largest optical depth along the sightline. The upper limit is set by the position of the CIV 1550Å line. The lower limit is extended by 100 km s^{-1} if $\tau > 0.1$ anywhere in the extension region; in practice the largest window for an absorber was $-700 < v < 250 \text{ km s}^{-1}$. This procedure follows Cooksey et al. (2013) as closely as possible. We also considered a fixed velocity interval of $-500 < v < 250 \text{ km s}^{-1}$, with negligible change to our results.

Figure 11 compares our simulated spectra to Cooksey et al. (2013). We show the observed line density per unit absorption distance, dN/dX , where X is the absorption distance defined in Eq. 5. We show dN/dX for absorbers with $W_{1548} > 0.3$ and $W_{1548} > 0.6 \text{ \AA}$. Sightlines with a CIV equivalent width of 0.3 \AA have a median $N_{\text{CIV}} \sim 5 \times 10^{14} \text{ cm}^{-2}$ (integrated along the entire sightline) in our simulations.

For both thresholds, the Illustris simulation produces less CIV than is observed by a factor of 3 at $z = 2$ and a factor of 5 at $z = 3.5$. The smaller and larger Illustris boxes, ILLUS 75 and ILLUS 25, which have identical feedback models, give similar results for $z < 3$, indicating good convergence with box size at these redshifts. At higher redshifts the smaller box produces noticeably fewer CIV absorbers. As discussed in Section 3, these strong absorbers arise close to haloes which are relatively large for this redshift ($10^{11} - 10^{12} h^{-1} M_{\odot}$), and the smaller box does not contain enough volume to sample this halo mass range completely.

By contrast, WARM and FAST, which employ more energetic wind models, each provide a good match to the observed $dN/dX(W > 0.3)$. The increased enrichment is more pronounced at higher redshifts, where a larger proportion of star formation is found in small haloes. These haloes have shallower potential wells, allowing more expulsion of metals. Thus FAST and WARM also better match the observed redshift evolution of $dN/dX(W > 0.6)$. However, even our more energetic wind models produce too few systems with an equivalent width greater than 0.6 \AA .

At $z < 2.5$, FAST has a lower $dN/dX(W_{1548} > 0.6)$ than WARM. This is due to the inclusion of AGN feedback in FAST and ILLUS, but not WARM. AGN feedback heats the gas in large halos above the 10^5 K where it can form CIV. We checked the effect of AGN feedback explicitly using two otherwise identical simulations³, and confirmed that it can substantially suppress CIV production at $z < 2.5$ and $W_{1548} > 0.3 \text{ \AA}$. Note that FAST has a larger $dN/dX(W_{1548} > 0.3)$ than WARM at $z > 2.5$.

Figure 12 shows the equivalent width distributions from the simulations, compared to the measurements of Cooksey et al. (2013). We define the equivalent width distribution, $f(W_{1548})$, analogously to the column density distribution, as the number of absorbers in a given equivalent width bin, $N(W_{1548})$, per unit equivalent width per unit absorption distance, ΔX (Eq. 5):

$$f(W_{1548}) = \frac{N(W_{1548})}{\Delta W_{1548} \Delta X(z)}. \quad (8)$$

We show the equivalent width distribution at two redshifts: $z = 2$ and $z = 3.5$. WARM and FAST both agree with the observations for $W_{1548} < 0.6 \text{ \AA}$ at $z = 3.5$ and $W_{1548} < 0.3 \text{ \AA}$ at $z = 2$. At $z = 2$ agreement between WARM and the observations is good except for the strongest absorbers, but all other simulations have too few systems by an order of magnitude. The agreement between WARM and the shape of the equivalent width distribution is remarkable, especially given that it lacks AGN feedback. At $z = 3.5$ the WARM and FAST models, while similar, are not a good match to observations for $W_{1548} > 0.6 \text{ \AA}$. The similarity between WARM and FAST indicates that the lack of AGN feedback in WARM is not having a significant effect at $z > 3$. At $z = 3.5$ the 25 Mpc/h simulations have reduced numbers of strong CIV absorbers due to their small simulation volume. However, the discrepancy between WARM and the observations is larger than the difference between the 25 and 75 Mpc/h boxes, indicating that a larger WARM box is unlikely to fully explain the discrepancy with observations.

Overall, both dN/dX and $f(W_{1548})$ paint a similar picture; good agreement between WARM and the observations for absorbers with $W_{1548} < 0.3 \text{ \AA}$, but a lack of the strongest absorbers, especially at $z = 3.5$. Interestingly, we showed in Figure 10 that other modern simulations, EAGLE and that of Oppenheimer et al. (2012), produce slightly fewer strong absorbers than WARM. Given this, we expect that both simulations would also under-produce CIV absorbers with equivalent widths $W_{1548} > 0.6 \text{ \AA}$, as we do, suggesting that the lack of large equivalent width absorbers in our simulations is a generic problem with modern feedback models.

³ HVEL and HVNOAGN from Bird et al. (2014)

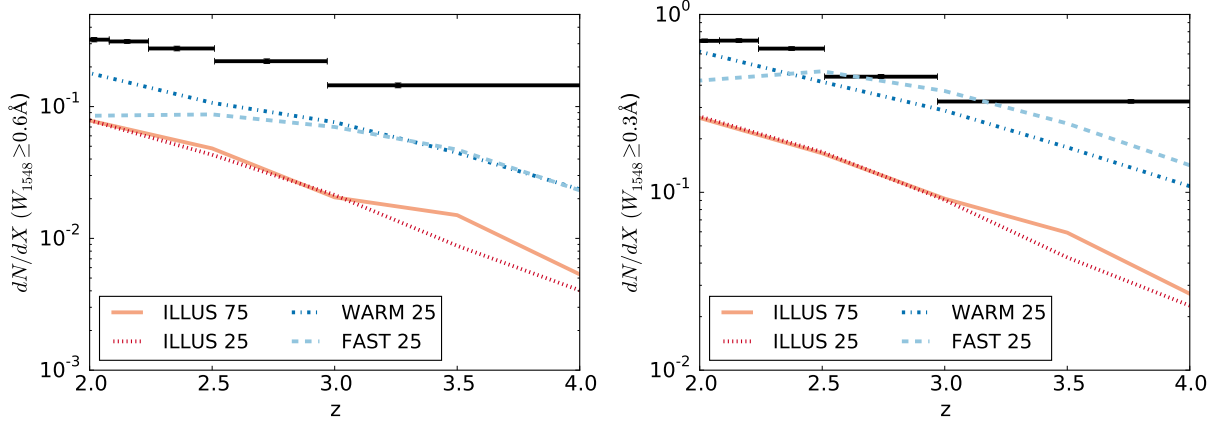


Figure 11. The line density of CIV extracted from our simulations at two different equivalent width thresholds, compared to the results of Cooksey et al. (2013). Left: with $W_{1548} > 0.6 \text{ \AA}$. Right: with $W_{1548} > 0.3 \text{ \AA}$. Statistical error bars are included for the observations. Cooksey et al. (2013) may also systematically underestimate the true dN/dX for $W_{1548} > 0.3 \text{ \AA}$ by $\sim 10\%$, due to the difficulty of detecting weak absorbers in SDSS spectra (Cooksey, private communication). Both statistical and systematic errors are small compared to the differences induced by our feedback models.

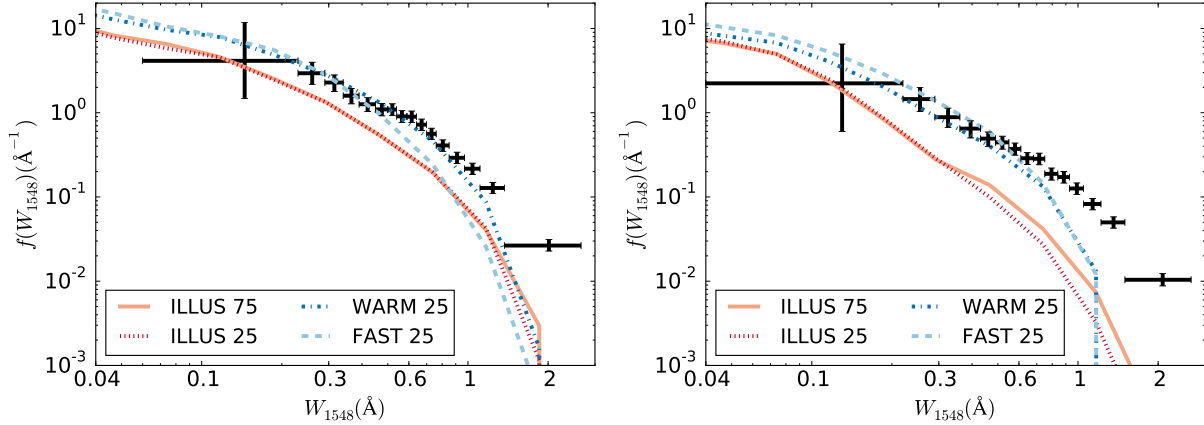


Figure 12. The equivalent width distribution of CIV extracted from our simulations, compared to the results of Cooksey et al. (2013). Left: at $z = 2$. Right: At $z = 3.5$. As with the line density, warmer or faster winds are in substantially better agreement with observations than Illustris. Note that sightlines with $N_{\text{CIV}} = 10^{15} \text{ cm}^{-2}$, the upper limit used in Figure 9, have a median equivalent width of $W_{1548} \approx 0.5 \text{ \AA}$ in our simulations.

Most absorbers with $W > 0.6 \text{ \AA}$ are found around haloes with masses $10^{11} - 10^{12} h^{-1} M_{\odot}$ (see Figure 4). A common feature of all current supernova feedback models is that they become ineffective at suppressing star formation in high mass haloes (e.g. Vogelsberger et al. 2013), motivating the need for AGN feedback. The reason behind this is that the deeper potential wells of these haloes render the supernova feedback models unable to expel gas from star-forming regions. It seems that matching the abundance of $W_{1548} > 0.6 \text{ \AA}$ absorbers also requires additional gas to be expelled from star-forming regions in large haloes. This could perhaps be achieved by stellar feedback models which are still efficient in larger haloes, or by modifying the AGN feedback to expel gas without heating it beyond 10^5 K .

4.3 Carbon absorption near Damped Lyman- α Systems

The equivalent widths of CIV and CII around DLAs were recently measured by Rubin et al. (2015). We have shown above that our simulations differ in the extent to which they expel metals into the circumgalactic medium, and DLAs are a tracer of the low-mass galaxy population at $z = 2 - 4$. Comparisons with the enrichment around DLAs thus seems a promising way to observationally constrain feedback models. It further provides a test of our conclusions in Sections 4.1 and 4.2 by partially isolating the effects on smaller haloes. All our feedback models produce similar populations of DLAs, in good agreement with observations (Bird et al. 2014, 2015). In particular, they match the observed DLA metallicity distribution and produce DLA host haloes with realistic virial velocities. We find that the majority of DLAs are found within haloes of mass $5 \times 10^9 - 10^{11} h^{-1} M_{\odot}$, and virial velocities $50 - 150 \text{ km s}^{-1}$.

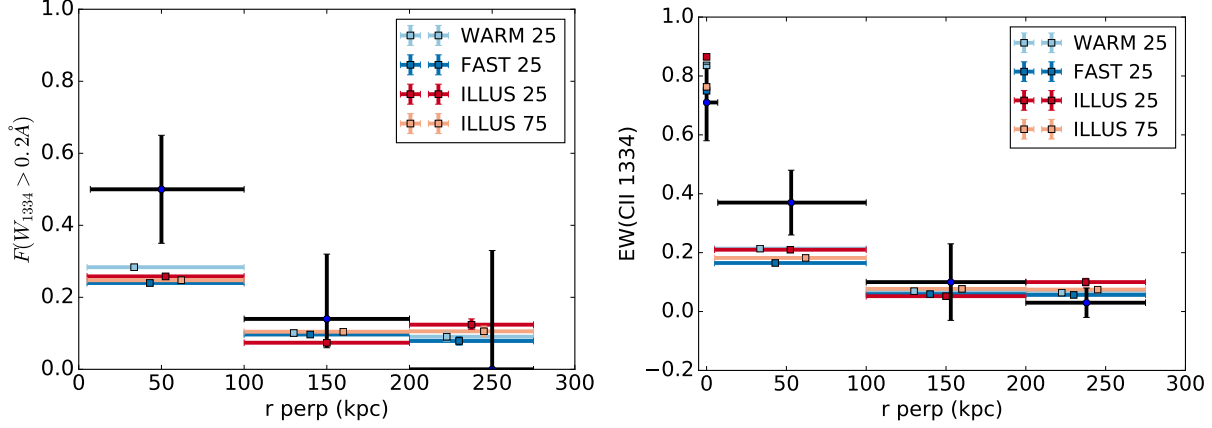


Figure 13. Covering fractions (Left) and mean equivalent widths (Right) of CII in 100 kpc wide impact parameter bins around DLAs, compared to the observations of Rubin et al. (2015) (black error bars). Bin centroids are offset for clarity. Vertical error bars on the simulations are generated using bootstrap resampling and show that the effect of sample variance is negligible. Points at $r_{\text{perp}} = 0$ indicate the equivalent width at the DLA.

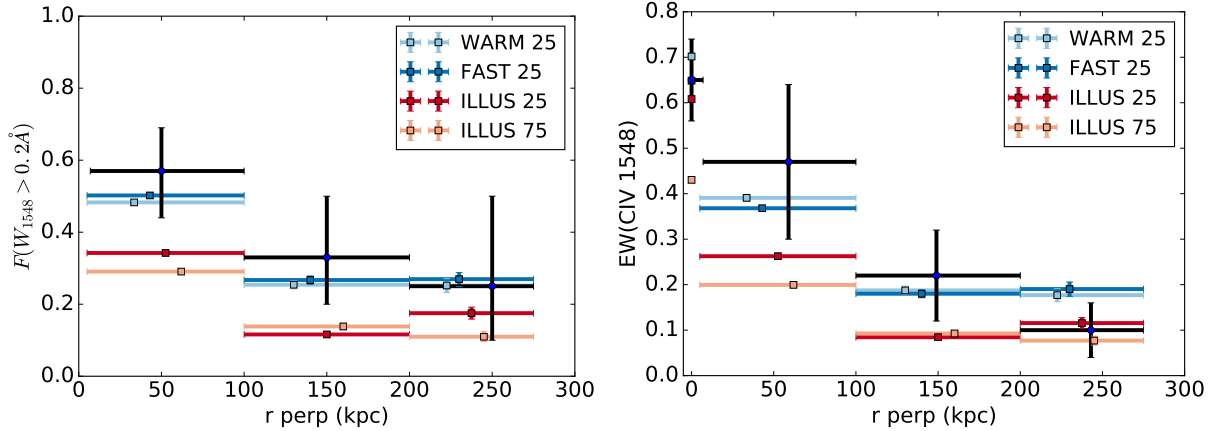


Figure 14. Covering fractions (Left) and mean equivalent widths (Right) of CIV in 100 kpc wide impact parameter bins around DLAs, compared to the observations of Rubin et al. (2015) (black error bars). Bin centroids are offset for clarity. Vertical error bars on the simulations are generated using bootstrap resampling and show that the effect of sample variance is negligible. Points at $r_{\text{perp}} = 0$ indicate the equivalent width at the DLA.

Rubin et al. (2015) obtained spectra from 40 quasar pairs and lensed quasars with sightlines separated by 7.5 to 275 kpc (physical). These pairs were selected so that a DLA was present in one sightline of the pair. Measurements of absorbers at the redshift of the DLA in the non-DLA sightline can thus constrain the state of the gas surrounding the DLA. As in previous sections, we generated a synthetic sightline catalogue similar to that observed. We first selected sightlines containing DLAs. The DLAs observed by Rubin et al. (2015) are concentrated at redshifts $z = 2-3$, so we selected sightlines from our snapshots at $z = 2, 2.5$ and 3 weighted to match the observed redshift distribution. For each of these DLAs we chose a sightline with a random impact parameter. The distribution of impact parameters was constrained to match the observed sample in each redshift bin, although in practice this was less important than matching the observed redshift distribution. Our simulated sample contained a total of 14,000 quasar pairs containing a DLA.

We computed equivalent widths following the method of

Rubin et al. (2015) as far as possible. We found the strongest HI absorption in the CGM sightline within $\pm 600 \text{ km s}^{-1}$ of the DLA redshift. Rubin et al. (2015) estimated, by eye, the velocity extent of this single HI absorption component and looked within this region for a strong metal line. We mimic this by choosing a region initially 400 km s^{-1} across, the mean size of the by-eye search window chosen in the observations, and extending it as needed in 100 km s^{-1} increments until we encounter a region without significant Lyman- α absorption, defined as a mean HI optical depth $\tau_{\text{HI}} > 0.1$ in the new 100 km s^{-1} region. We then examine this region to find the strongest metal line and defined the equivalent width to be the integral within $\pm 300 \text{ km s}^{-1}$ around line centre. Note that this procedure gave results comparable to defining the equivalent width to be the integral of the metal line absorption within $\pm 600 \text{ km s}^{-1}$ of the DLA.

Figure 13 shows the covering fractions of CII systems with $W_{1334} > 0.2 \text{ \AA}$, $F(W_{1334} > 0.2)$, and the mean CII equivalent widths, for sightlines around DLAs.

CII traces cooler, denser gas than CIV, more closely associated with a DLA or a Lyman Limit System. This cold gas is insensitive to the differences between our feedback models; the outflowing gas shock-heats and so yields negligible CII absorption in any case. Thus all our simulations give very similar results, in good agreement with the observational measurements at $r_{\text{perp}} > 100$ kpc, but $1 - 2\sigma$ discrepant at $r_{\text{perp}} < 100$ kpc. The good agreement of the simulations at larger perpendicular distances is another useful validation of our underlying model. The moderately low CII equivalent width nearer the DLA predicted in our models, combined with the overly large value of Ω_{DLA} at $z = 2$ noted in Bird et al. (2014), may suggest that the feedback model needs to further suppress cold gas in small haloes. This would cause the median DLA to reside in a slightly more massive halo, slightly boosting its metallicity, and thus CII abundance. However, the significance of the discrepancy is not high, and it could simply be a statistical fluctuation, especially as the models are in good agreement with the observed CII equivalent width within the DLAs. We have also checked that all our simulations give similar results for the observed covering fractions of SiII and SiIV around DLAs, in good agreement with the observations of Rubin et al. (2015).

Figure 14 shows the covering fractions of CIV systems with $W_{1548} > 0.2$ Å, $F(W_{1548} > 0.2)$, and the mean CIV equivalent widths, for sightlines around DLAs. The CIV statistics are sensitive to the differences between our feedback models, and the more energetic winds in WARM and FAST are again in better agreement with observations than the default Illustris model, especially near the DLA. We have checked that the increased CIV equivalent width owes to a larger column density, rather than increased thermal or velocity broadening in existing lines. In the bin farthest from the DLA, the WARM simulation slightly overpredicts the mean CIV equivalent width, but we do not regard this as significant, especially as the CIV covering fraction in the same bin is in good agreement with observations. The tension between the Illustris feedback model and the observed CIV statistics is relatively weak, but certainly significant, especially when considered with the results of earlier sections. The statistics of CIV around DLAs thus also favour the WARM and FAST feedback models, and extend our conclusions by isolating the effect of the feedback model on the smaller halos which host DLAs.

5 CONCLUSIONS

We have compared our simulations to three different carbon absorber measurements at $z = 2 - 4$, with the aim of constraining a parameter of the Illustris feedback model. Two are blind CIV surveys; the column density distribution function (CDDF) of CIV absorbers from D’Odorico et al. (2010) and the equivalent width distribution of (stronger) CIV absorbers from Cooksey et al. (2013). The third measurement is a CIV and CII absorption survey around DLAs from Rubin et al. (2015). We compared to the Illustris simulation and some smaller simulations with modified feedback models. Motivated by the results of Suresh et al. (2015b), our feedback models were modified to have more energetic winds, realised by an increased wind velocity or an increased wind thermal energy. Our modifications to the Illustris feed-

back model were chosen so that they did not alter the good agreement with the observed galaxy stellar mass function.

We demonstrated that, nevertheless, our more energetic feedback models affected the CDDF and equivalent width distributions of CIV at a level highly significant compared to the observational error bars, and the distribution of CIV around DLAs at a level comparable to the error bars. All measurements favoured the more energetic wind models, which were better able to enrich the gas surrounding haloes. There is little difference between the model with an increased wind velocity and that with increased thermal energy, so we do not favour one over the other, both being in generally good agreement with observations. The Illustris feedback model did not sufficiently enrich the gas surrounding galaxies, and under-produced CIV in all the observational measurements we compared to. Furthermore, Suresh et al. (2015b) found that a larger wind energy per unit mass moderately improves agreement with the radial profile of CIV around Lyman break galaxies (LBGs) (Turner et al. 2014). All wind models produce similar results for the CII around DLAs, which is in reasonable good agreement with observations, being discrepant at the $1.5 - \sigma$ level in only one projected radial bin near the DLA.

We were not able to reproduce the abundance of the strongest CIV absorbers with equivalent widths $W_{1548} > 0.6$ Å. The SDSS spectra within which these absorbers are detected are low resolution and of relatively low signal to noise. They may thus suffer from various observational systematics, including blending with other metal lines or poor continuum estimation. However, to completely reconcile our results, these effects would have to be large; we under-produce $W_{1548} \sim 1$ Å absorbers by almost an order of magnitude.

Our simulations thus still appear to suffer from a generic lack of CIV absorbers with the highest column densities. It may be possible to resolve this discrepancy by further increasing the energy per unit mass of the wind model. To avoid over-producing lower column densities or reducing the stellar mass function below the range allowed by observations, such a change would need to be targeted at $10^{11} - 10^{12} h^{-1} M_{\odot}$ halos, a mass range where supernova winds struggle to escape their halos. Alternatively, since these strong absorbers are saturated, it may be possible to achieve better agreement with observations by increasing the velocity dispersion of the absorbing gas rather than the CIV column density; in this case it would be necessary to avoid heating the gas substantially above 10^5 K and further ionizing carbon. A final possibility could be a modification of the AGN feedback model to enrich the gas without heating it beyond 10^5 K.

Rahmati et al. (2015) measured the CIV column density function in the EAGLE Project, a recent simulation using purely thermal supernova feedback models. We performed a comparison of the results of the EAGLE project, as well as the simulations of Oppenheimer et al. (2012), to ours. While both simulations, Oppenheimer et al. (2012) especially, were a reasonable match to the CIV CDDF, they both produced fewer strong absorbers than our most energetic wind models. Given this, we expect that both simulations would also under-produce CIV absorbers with equivalent widths $W_{1548} > 0.6$ Å, as we do, suggesting that the

lack of large equivalent width absorbers in our simulations is a generic problem with modern feedback models.

We examined some properties of the CIV absorbers, including their host halos, their distribution within a halo, and their collisional ionization fraction. We found that CIV absorbers are found throughout halos, even substantially beyond their virial radius, while CII absorbers are generally confined to the high density gas near the inner regions of the halo. The strongest CIV absorbers with $W_{1548} > 0.5 \text{ \AA}$ are however associated with the interiors of the larger haloes. Especially in the simulations with stronger winds, CIV absorbers of all strengths arise predominantly from photoionized gas at $z = 2 - 3$.

This paper should be viewed in the context of our previous work (Bird et al. 2014), which showed that the Illustris simulation reproduces the statistics of strong neutral hydrogen absorbers. We showed there that the fast and warm winds considered in this paper produce a very similar population of neutral hydrogen absorbers to the default Illustris model, and we showed here that they do not affect the galaxy stellar mass function. This thus demonstrates that CIV absorbers are able to constrain the Illustris feedback model parameters in a way independent to either of these quantities. Taken together, these papers may indicate that it is possible to calibrate a feedback model to high redshift absorption line statistics, rather than the more usual low redshift stellar mass function. Absorption lines can probe low-mass objects at high redshift whose stellar components are not directly observable. Furthermore, they have very different systematic errors from galaxy stellar mass functions. We may return to this in future work.

Overall, we recommend that designers of future supernova feedback models explicitly check whether they match the observed properties of CIV in the intergalactic medium or around galaxies. Models which include winds with sufficient energy to allow metals to easily escape galactic haloes and enrich their environment seem likely to provide a reasonable match to the CIV CDDF, as shown both in our results and those of Oppenheimer et al. (2012). While the Illustris model is somewhat discrepant, we showed that our warm and fast wind models produce gas around relatively low-mass haloes in good agreement with the CIV CDDF, and the distribution of CIV and CII around DLAs. However, they under-produce the number of CIV absorbers with $W_{1548} > 0.6 \text{ \AA}$, necessitating some further modification of the feedback model.

APPENDIX A: RESOLUTION CONVERGENCE

In this Appendix, we will consider how our results are affected by the resolution of the simulation. Computational limits prevent us from performing a simulation with the same box size and double the resolution of our fiducial box. Instead we have performed a simulation which uses the Illustris feedback model, but reduces the box size to 7.5 Mpc. The particle load remains constant at 512^3 , thus increasing the mass resolution by a factor of ~ 40 . Unfortunately, the 7.5 Mpc box artificially suppresses the number of absorbers with $N_{\text{CIV}} > 10^{14} \text{ cm}^{-2}$ because it is insufficiently large to include many of the more massive halos. The largest halo in the 7.5 Mpc/h box has mass $M = 2.7 \times 10^{11} M_{\odot}/h$, while the

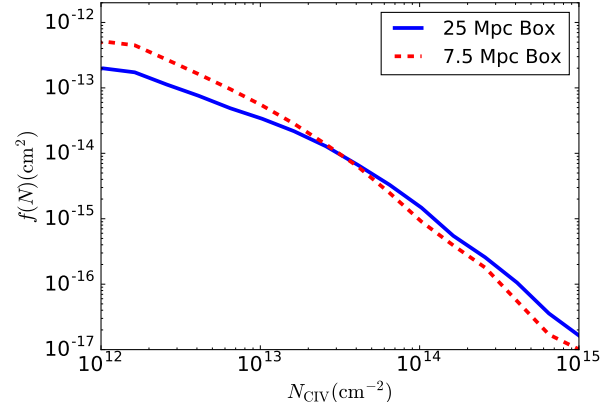


Figure A1. A comparison of the CIV column density distribution from our 25 Mpc Illustris feedback model simulation and an identical 7.5 Mpc box with higher resolution. To limit the effect of the smaller box, we have removed from the column density function spectra near halos with $M > 2.7 \times 10^{11} M_{\odot}/h$, the mass of the largest halo in the smaller box. We caution that for $N_{\text{CIV}} > 10^{14} \text{ cm}^{-2}$, over 90% of the absorbers in the larger box are associated with halos with mass $M > 10^{11} M_{\odot}/h$, of which there are only 8 in the smaller box.

largest halo in the 25 Mpc/h box has $M = 2 \times 10^{12} M_{\odot}/h$. To limit the effect of these larger halos, we exclude from the sample all spectra from the 25 Mpc box associated with halos with mass $M = 2.7 \times 10^{11} M_{\odot}/h$. Figure A1 shows the resulting CIV CDDF for both boxes. The small box reduces the number of CIV absorbers with $N_{\text{CIV}} > 10^{14} \text{ cm}^{-2}$ by a factor of two. This difference is most likely due to the reduced box size; over 90% of the CDDF in the 25 Mpc/h box comes from absorbers associated with halos with mass $M > 10^{11} M_{\odot}/h$. This mass range includes only 8 halos in the 7.5 Mpc/h box, and so the sample size is still insufficient.

The increase in resolution in the 7.5 Mpc/h box increases the number of absorbers with $N_{\text{CIV}} < 10^{13} \text{ cm}^{-2}$ by up to 50%. This arises from the increase in the global star formation rate from resolving smaller halos. The smaller box resolves halos down to $10^9 M_{\odot}/h$, and thus includes essentially all halos able to form stars against the thermal pressure of the ionized intergalactic medium. Compared to the differences between our Illustris and WARM feedback models, the increase with higher resolution is relatively mild. It is interesting to note that a correction of this size, applied to the WARM model, would substantially improve agreement with observations.

We do not show resolution convergence for the equivalent width distribution shown in Section 4.2, as these strong absorbers are found almost exclusively in halos more massive than those in the 7.5 Mpc box.

APPENDIX B: TABULATED RESULTS

In this Appendix we provide our results in tabulated form. Table B1 gives the CIV CDDF from Figure 9, and Table B2 gives the evolution of Ω_{CIV} . Tables B4 and B3 give the equivalent width distributions of strong absorbers from Figure 12 at $z = 3.5$ and $z = 2$ respectively. Table B5 shows

$N_{\text{CIV}} \text{ (cm}^{-2}\text{)}$	WARM	FAST	ILLUS 75
1.0×10^{12}	5.6×10^{-13}	7.3×10^{-13}	4.1×10^{-13}
1.6×10^{12}	4.3×10^{-13}	5.6×10^{-13}	2.9×10^{-13}
2.6×10^{12}	2.6×10^{-13}	3.3×10^{-13}	1.7×10^{-13}
4.1×10^{12}	1.7×10^{-13}	2.1×10^{-13}	1.1×10^{-13}
6.5×10^{12}	1.0×10^{-13}	1.3×10^{-13}	7.2×10^{-14}
1.0×10^{13}	6.7×10^{-14}	8.2×10^{-14}	4.4×10^{-14}
1.6×10^{13}	4.0×10^{-14}	5.2×10^{-14}	2.8×10^{-14}
2.6×10^{13}	2.6×10^{-14}	3.3×10^{-14}	1.7×10^{-14}
4.1×10^{13}	1.6×10^{-14}	1.9×10^{-14}	9.5×10^{-15}
6.5×10^{13}	8.9×10^{-15}	1.1×10^{-14}	5.2×10^{-15}
1.0×10^{14}	5.1×10^{-15}	6.6×10^{-15}	2.4×10^{-15}
1.6×10^{14}	2.9×10^{-15}	3.5×10^{-15}	1.2×10^{-15}
2.6×10^{14}	1.5×10^{-15}	1.6×10^{-15}	5.3×10^{-16}
4.1×10^{14}	7.4×10^{-16}	7.0×10^{-16}	2.6×10^{-16}
6.5×10^{14}	3.8×10^{-16}	2.9×10^{-16}	1.2×10^{-16}
1.0×10^{15}	1.6×10^{-16}	1.0×10^{-16}	6.3×10^{-17}

Table B1. CIV CDDF $f(N)$ in cm^2 for our simulations.

z	FAST	ILLUS 75	WARM
4.00	1.79	0.47	1.33
3.50	2.74	0.78	2.00
3.00	4.01	1.12	3.02
2.50	5.36	1.85	4.29
2.00	5.31	2.61	6.07

Table B2. $\Omega_{\text{CIV}} \times 10^8$ for our simulations.

Figure 11, the evolution of dN/dX ($W_{1548} > 0.6 \text{ \AA}$) with redshift.

ACKNOWLEDGEMENTS

We thank Valentina D’Odorico for sharing her data on the CIV column density function, Ben Oppenheimer and Ali Rahmati for sharing CIV column density tables from their simulations with us, J. X. Prochaska for reading a draft and providing thoughtful comments, and Volker Springel for writing and allowing us to use the AREPO code. We also thank Kathy Cooksey for sharing her data on the CIV equivalent width function, for many interesting discussions and for proof-reading a draft. SB was supported by NASA through Einstein Postdoctoral Fellowship Award Number PF5-160133 and by a McWilliams Fellowship from

$W_{1548} \text{ (\AA)}$	FAST	ILLUS 75	WARM
4.7×10^{-2}	15.22	8.29	12.79
7.4×10^{-2}	10.58	6.54	9.67
0.12	8.02	4.58	7.89
0.19	5.61	2.56	4.91
0.29	2.81	1.33	2.82
0.47	0.97	0.54	1.32
0.74	0.24	0.20	0.46
1.17	2.6×10^{-2}	4.0×10^{-2}	8.7×10^{-2}
1.85	4.3×10^{-4}	3.0×10^{-3}	1.6×10^{-3}

Table B3. Equivalent width distributions, $f(W_{1548}) \text{ (\AA}^{-1}\text{)}$, for our simulations at $z = 2$.

$W_{1548} \text{ (\AA)}$	FAST	WARM	ILLUS 75
4.7×10^{-2}	10.40	8.20	6.68
7.4×10^{-2}	8.27	6.76	5.00
0.12	5.26	4.02	2.32
0.19	2.90	2.04	0.84
0.29	1.36	0.89	0.28
0.47	0.60	0.40	0.14
0.74	0.15	0.13	4.2×10^{-2}
1.17	1.2×10^{-2}	1.3×10^{-2}	7.4×10^{-3}
1.85	0	0	3.3×10^{-4}

Table B4. Equivalent width distributions, $f(W_{1548}) \text{ (\AA}^{-1}\text{)}$, for our simulations at $z = 3.5$.

z	WARM	ILLUS 75	FAST
4.00	2.4×10^{-2}	5.3×10^{-3}	2.3×10^{-2}
3.50	4.4×10^{-2}	1.5×10^{-2}	4.7×10^{-2}
3.00	7.6×10^{-2}	2.0×10^{-2}	7.0×10^{-2}
2.50	0.11	4.8×10^{-2}	8.7×10^{-2}
2.00	0.18	7.8×10^{-2}	8.5×10^{-2}

Table B5. dN/dX ($W_{1548} > 0.6 \text{ \AA}$) for our simulations.

Carnegie Mellon University. LH is supported by NASA ATP Award NNX12AC67G and NSF grant AST-1312095.

REFERENCES

- Bahcall J. N., Peebles P. J. E., 1969, ApJL, 156, L7, doi:10.1086/180337
- Barai P. et al., 2013, MNRAS, 430, 3213, arXiv:1210.3582, doi:10.1093/mnras/stt125
- Becker G. D., Rauch M., Sargent W. L. W., 2009, ApJ, 698, 1010, arXiv:0812.2856, doi:10.1088/0004-637X/698/2/1010
- Bird S., Vogelsberger M., Haehnelt M., Sijacki D., Genel S., Torrey P., Springel V., Hernquist L., 2014, MNRAS, 445, 2313, arXiv:1405.3994, doi:10.1093/mnras/stu1923
- Bird S., Haehnelt M., Neeleman M., Genel S., Vogelsberger M., Hernquist L., 2015, MNRAS, 447, 1834, arXiv:1407.7858, doi:10.1093/mnras/stu2542
- Boksenberg A., Sargent W. L. W., Rauch M., 2003, in Perez E., Gonzalez Delgado R. M., Tenorio-Tagle G., eds, Astronomical Society of the Pacific Conference Series Vol. 297, Star Formation Through Time. p. 447
- Burchett J. N., Tripp T. M., Werk J. K., Howk J. C., Prochaska J. X., Ford A. B., Davé R., 2013, ApJL, 779, L17, arXiv:1311.4559, doi:10.1088/2041-8205/779/2/L17
- Burchett J. N. et al., 2015, ApJ, 815, 91, arXiv:1510.01329, doi:10.1088/0004-637X/815/2/91
- Cen R., Chisari N. E., 2011, ApJ, 731, 11, arXiv:1005.1451, doi:10.1088/0004-637X/731/1/11
- Chabrier G., 2003, PASP, 115, 763, arXiv:astro-ph/0304382, doi:10.1086/376392
- Cooksey K. L., Thom C., Prochaska J. X., Chen H.-W., 2010, ApJ, 708, 868, arXiv:0906.3347, doi:10.1088/0004-637X/708/1/868

- Cooksey K. L., Kao M. M., Simcoe R. A., O'Meara J. M., Prochaska J. X., 2013, *ApJ*, 763, 37, arXiv:1204.2827, doi:10.1088/0004-637X/763/1/37
- Crighton N. H. M., Hennawi J. F., Simcoe R. A., Cooksey K. L., Murphy M. T., Fumagalli M., Prochaska J. X., Shanks T., 2015, *MNRAS*, 446, 18, arXiv:1406.4239, doi:10.1093/mnras/stu2088
- D'Odorico V., Calura F., Cristiani S., Viel M., 2010, *MNRAS*, 401, 2715, arXiv:0910.2126, doi:10.1111/j.1365-2966.2009.15856.x
- Danforth C. W., Shull J. M., 2008, *ApJ*, 679, 194, arXiv:0709.4030, doi:10.1086/587127
- Davé R., Oppenheimer B. D., Katz N., Kollmeier J. A., Weinberg D. H., 2010, *MNRAS*, 408, 2051, arXiv:1005.2421, doi:10.1111/j.1365-2966.2010.17279.x
- Davé R., Oppenheimer B. D., Finlator K., 2011, *MNRAS*, 415, 11, arXiv:1103.3528, doi:10.1111/j.1365-2966.2011.18680.x
- Di Matteo T., Springel V., Hernquist L., 2005, *Nature*, 433, 604, arXiv:astro-ph/0502199, doi:10.1038/nature03335
- Faucher-Giguère C.-A., Lidz A., Zaldarriaga M., Hernquist L., 2009, *ApJ*, 703, 1416, arXiv:0901.4554, doi:10.1088/0004-637X/703/2/1416
- Ferland G. J. et al., 2013, *RMXAA*, 49, 137, arXiv:1302.4485
- Ford A. B., Oppenheimer B. D., Davé R., Katz N., Kollmeier J. A., Weinberg D. H., 2013, *MNRAS*, 432, 89, doi:10.1093/mnras/stt393
- Ford A. B., Davé R., Oppenheimer B. D., Katz N., Kollmeier J. A., Thompson R., Weinberg D. H., 2014, *MNRAS*, 444, 1260, arXiv:1309.5951, doi:10.1093/mnras/stu1418
- Genel S., Vogelsberger M., Nelson D., Sijacki D., Springel V., Hernquist L., 2013, *MNRAS*, 435, 1426, arXiv:1305.2195, doi:10.1093/mnras/stt1383
- Genel S. et al., 2014, *MNRAS*, 445, 175, arXiv:1405.3749, doi:10.1093/mnras/stu1654
- Haehnelt M. G., Steinmetz M., Rauch M., 1996, *ApJL*, 465, L95, arXiv:astro-ph/9512118, doi:10.1086/310156
- Keating L. C., Puchwein E., Haehnelt M. G., Bird S., Bolton J. S., 2016, *MNRAS*, 461, 606, arXiv:1603.03332, doi:10.1093/mnras/stw1306
- Marinacci F., Pakmor R., Springel V., 2014, *MNRAS*, 437, 1750, arXiv:1305.5360, doi:10.1093/mnras/stt2003
- Mortlock A., Conselice C. J., Bluck A. F. L., Bauer A. E., Grützbauch R., Buitrago F., Ownsworth J., 2011, *MNRAS*, 413, 2845, arXiv:1101.2867, doi:10.1111/j.1365-2966.2011.18357.x
- Nelson D. et al., 2015, *Astronomy and Computing*, 13, 12, arXiv:1504.00362, doi:10.1016/j.ascom.2015.09.003
- Okamoto T., Frenk C. S., Jenkins A., Theuns T., 2010, *MNRAS*, 406, 208, arXiv:0909.0265, doi:10.1111/j.1365-2966.2010.16690.x
- Oppenheimer B. D., Davé R., 2006, *MNRAS*, 373, 1265, arXiv:astro-ph/0605651, doi:10.1111/j.1365-2966.2006.10989.x
- Oppenheimer B. D., Davé R., 2008, *MNRAS*, 387, 577, arXiv:0712.1827, doi:10.1111/j.1365-2966.2008.13280.x
- Oppenheimer B. D., Schaye J., 2013, *MNRAS*, 434, 1043, arXiv:1302.5710, doi:10.1093/mnras/stt1043
- Oppenheimer B. D., Davé R., Katz N., Kollmeier J. A., Weinberg D. H., 2012, *MNRAS*, 420, 829, arXiv:1106.1444, doi:10.1111/j.1365-2966.2011.20096.x
- Pettini M., Madau P., Bolte M., Prochaska J. X., Ellison S. L., Fan X., 2003, *ApJ*, 594, 695, arXiv:astro-ph/0305413, doi:10.1086/377043
- Puchwein E., Springel V., 2013, *MNRAS*, 428, 2966, arXiv:1205.2694, doi:10.1093/mnras/sts243
- Rahmati A., Pawlik A. H., Raicevic M., Schaye J., 2013, *MNRAS*, 430, 2427, arXiv:1210.7808, doi:10.1093/mnras/stt066
- Rahmati A., Schaye J., Bower R. G., Crain R. A., Furlong M., Schaller M., Theuns T., 2015, *MNRAS*, 452, 2034, arXiv:1503.05553, doi:10.1093/mnras/stv1414
- Rahmati A., Schaye J., Crain R. A., Oppenheimer B. D., Schaller M., Theuns T., 2016, *MNRAS*, 459, 310, arXiv:1511.01094, doi:10.1093/mnras/stw453
- Rubin K. H. R., Hennawi J. F., Prochaska J. X., Simcoe R. A., Myers A., Lau M. W., 2015, *ApJ*, 808, 38, arXiv:1411.6016, doi:10.1088/0004-637X/808/1/38
- Ryan-Weber E. V., Pettini M., Madau P., Zych B. J., 2009, *MNRAS*, 395, 1476, arXiv:0902.1991, doi:10.1111/j.1365-2966.2009.14618.x
- Scannapieco E., Pichon C., Aracil B., Petitjean P., Thacker R. J., Pogosyan D., Bergeron J., Couchman H. M. P., 2006, *MNRAS*, 365, 615, arXiv:astro-ph/0503001, doi:10.1111/j.1365-2966.2005.09753.x
- Schaye J. et al., 2010, *MNRAS*, 402, 1536, arXiv:0909.5196, doi:10.1111/j.1365-2966.2009.16029.x
- Schaye J. et al., 2015, *MNRAS*, 446, 521, arXiv:1407.7040, doi:10.1093/mnras/stu2058
- Shen S., Madau P., Aguirre A., Guedes J., Mayer L., Wadsley J., 2012, *ApJ*, 760, 50, arXiv:1109.3713, doi:10.1088/0004-637X/760/1/50
- Shen S., Madau P., Guedes J., Mayer L., Prochaska J. X., Wadsley J., 2013, *ApJ*, 765, 89, arXiv:1205.0270, doi:10.1088/0004-637X/765/2/89
- Sijacki D., Springel V., Di Matteo T., Hernquist L., 2007, *MNRAS*, 380, 877, arXiv:0705.2238, doi:10.1111/j.1365-2966.2007.12153.x
- Simcoe R. A. et al., 2011, *ApJ*, 743, 21, arXiv:1104.4117, doi:10.1088/0004-637X/743/1/21
- Songaila A., 2001, *ApJL*, 561, L153, arXiv:astro-ph/0110123, doi:10.1086/324761
- Songaila A., 2005, *AJ*, 130, 1996, arXiv:astro-ph/0507649, doi:10.1086/491704
- Springel V., 2010, *MNRAS*, 401, 791, arXiv:0901.4107, doi:10.1111/j.1365-2966.2009.15715.x
- Springel V., Hernquist L., 2003, *MNRAS*, 339, 289, arXiv:astro-ph/0206393, doi:10.1046/j.1365-8711.2003.06206.x
- Springel V., Di Matteo T., Hernquist L., 2005, *MNRAS*, 361, 776, arXiv:astro-ph/0411108, doi:10.1111/j.1365-2966.2005.09238.x
- Suresh J., Rubin K. H. R., Kannan R., Werk J. K., Hernquist L., Vogelsberger M., 2015a, *ArXiv e-prints*, arXiv:1511.00687
- Suresh J., Bird S., Vogelsberger M., Genel S., Torrey P., Sijacki D., Springel V., Hernquist L., 2015b, *MNRAS*, 448, 895, arXiv:1501.02267, doi:10.1093/mnras/stu2762
- Tescari E., Viel M., D'Odorico V., Cristiani S., Calura F., Borgani S., Tornatore L., 2011, *MNRAS*, 411, 826, arXiv:1007.1628, doi:10.1111/j.1365-2966.2010.17761.x
- Torrey P., Vogelsberger M., Genel S., Sijacki D.,

- Springel V., Hernquist L., 2014, MNRAS, 438, 1985, arXiv:1305.4931, doi:10.1093/mnras/stt2295
- Turner M. L., Schaye J., Steidel C. C., Rudie G. C., Strom A. L., 2014, MNRAS, 445, 794, arXiv:1403.0942, doi:10.1093/mnras/stu1801
- Vogelsberger M., Genel S., Sijacki D., Torrey P., Springel V., Hernquist L., 2013, MNRAS, 436, 3031, arXiv:1305.2913, doi:10.1093/mnras/stt1789
- Vogelsberger M. et al., 2014a, MNRAS, 444, 1518, arXiv:1405.2921, doi:10.1093/mnras/stu1536
- Vogelsberger M. et al., 2014b, Nature, 509, 177, arXiv:1405.1418, doi:10.1038/nature13316
- York D. G. et al., 2000, AJ, 120, 1579, arXiv:astro-ph/0006396, doi:10.1086/301513
- van Daalen M. P., Schaye J., Booth C. M., Dalla Vecchia C., 2011, MNRAS, 415, 3649, arXiv:1104.1174, doi:10.1111/j.1365-2966.2011.18981.x